Vapor Pressures of Low-Temperature C_2H_x Hydrocarbon Ices

W.M. Grundy[1,2], S.P. Tan[3], J.K. Steckloff[3,4], A.S. Smith[1], T.M. Lucas[1,2],
G.E. Lindberg[5,6], M.D. Brand[6], S.C. Tegler[1], C.L. Thieberger[1],
I.E. Knudsen[1], and J. Hanley[1,2]

1. Department of Astronomy and Planetary Science, Northern Arizona University, Flagstaff Arizona.
2. Lowell Observatory, Flagstaff Arizona.
3. Planetary Science Institute, Tucson Arizona.
4. Department of Aerospace Engineering and Engineering Mechanics, University of Texas at Austin, Austin Texas.
5. Center for Material Interfaces in Research and Applications, Northern Arizona University, Flagstaff Arizona.
6. Department of Chemistry and Biochemistry, Northern Arizona University, Flagstaff Arizona.

— in press in *Icarus* 2026 —

Keywords: *Ices; Planetary material thermodynamics; Experimental Techniques*; *Hydrocarbons*.

Abstract

Ethane (C_2H_6), ethylene (C_2H_4), and acetylene (C_2H_2) are cosmically abundant hydrocarbons with two carbon atoms. They play important roles in a variety of astrophysical settings from sublimation of cometary ices, to photolytic haze formation in the upper atmospheres of Titan and Pluto, to formation of Charon’s dark reddish polar cap, to chemical evolution of protoplanetary nebulae. Temperature-dependent vapor pressures and latent heats of sublimation of these species at relevant temperatures are needed to accurately model the processes involved. We used a quartz crystal microbalance to make new measurements of the sublimation rates of these hydrocarbon ices at low temperatures and pressures relevant to diverse environments. Our method accounts for simultaneous sublimation from and condensation onto the quartz crystal. We find vapor pressures of C_2H_6 and C_2H_4 ices to be similar to previous estimates in the literature, while the vapor pressure of C_2H_2 is much lower, owing to the existence of a second,

lower temperature solid phase stable below 133 K. We also provide updated parameters for ices of N_2, CO, CH_4, O_2, and NH_3 that we had previously published, applying a new correction to account for condensation from other cold parts of the apparatus.

Introduction

Hydrocarbon molecules featuring two carbon atoms are abundant in numerous Solar System and astrophysical settings. They have been detected in infrared reflectance spectra of icy dwarf planets Quaoar, Gonggong, Sedna, and Makemake (Emery et al. 2024; Protopapa et al. 2025). CH_4 that becomes cold-trapped on Charon's winter poles is photolyzed into C2 hydrocarbons that are subsequently processed into the material coloring its distinctive reddish poles (Grundy et al. 2016; Hoey et al. 2017; Raut et al. 2022; Teolis et al. 2022). C2 hydrocarbons are among the simplest product molecules from photochemistry in CH_4-rich N_2 atmospheres such as those of Titan (e.g., Hirtzig et al. 2009; Hörst 2017; Nixon 2024) and Pluto (e.g., Young et al. 2018; Gladstone & Young 2019; Lavvas et al. 2021). In addition to providing feedstock to build larger molecules (e.g., Hudson et al. 2009), they can play important roles in the condensation of haze or aerosol particles in those atmospheres (e.g., Tomasko et al. 2008; Cheng et al. 2017). After settling to the surface, C2 hydrocarbons are expected to become major constituents of Titan's lakes (e.g., Brown et al. 2008; Clark et al. 2010; Mastrogiuseppe 2018) and could participate in a variety of processes, such as the formation of evaporites (e.g., Cordier et al. 2013; Czaplinski et al. 2019). C2 hydrocarbons are observed in comets at varying abundances relative to water ice, pointing to the existence of chemically distinct formation environments in the Sun's proto-planetary nebula (e.g., Paganini et al. 2019; Bair & Schleicher 2025). JWST has detected C2 hydrocarbons in observations of protoplanetary disks around low mass stars (Arabhavi et al. 2024; Colmenares et al. 2024; Feng et al. 2025). A potentially important source is thermal destruction of carbonaceous grains in the hot, inner part of the disk (Tabone et al. 2023; Houge et al. 2025). C2 hydrocarbons can also be inherited from the cold molecular clouds from which protoplanetary disks collapse (e.g., Carrascosa et al. 2020).

The vapor pressure of a frozen volatile substance is the pressure at which the gas phase is in thermodynamic equilibrium with the solid phase, where condensation and sublimation rates are equal. Knowledge of the vapor pressures of C2 hydrocarbon ices as a function of temperature is needed for modeling their sublimation and condensation behavior in the many settings where they play important roles. Vapor pressure data for 27 different ice species were compiled by Fray and Schmitt (2009), including the three C2 hydrocarbons that are the focus of this paper. Fray & Schmitt reviewed published laboratory data and provided polynomial expressions for the vapor pressures as a function of temperature. However, they remarked that additional studies at lower temperatures were needed. For instance, the lowest temperatures having published vapor pressure measurements for C_2H_2, C_2H_4, and C_2H_6 ices were at 98.5 K, 77.3 K, and 80.8 K, respectively. In this paper, we report new measurements at lower temperatures for all three ices, and we provide new polynomial expressions fitted to the combination of new plus previously published data.

Methods

Our experimental method made use of a quartz crystal microbalance (QCM) as described in two previous papers (Blakley et al. 2024; Grundy et al. 2024). We used a QCM installed at the Astrophysical Materials Laboratory at Northern Arizona University. It is attached via a copper mount and angle bracket to the cold tip of a two stage closed cycle helium refrigerator, housed within a stainless steel ultra-high vacuum chamber that is cryopumped to a base pressure of ~10^{-9} Torr (10^{-7} Pa). See (Blakley et al. 2024; Grundy et al. 2024) for additional details. We vapor deposited a thin film of ice onto the QCM at low temperature, then increased the temperature and observed the areal mass loss rate as the ice sublimated. From mass loss rates measured at a series of temperatures, we derived the corresponding ice vapor pressures for those temperatures. We used separate measurements of the mass deposition rate as a function of chamber pressure to correct for simultaneous condensation onto the quartz crystal from residual gas in the vacuum chamber (Blakley et al. 2024). We have updated our data analysis in two crucial ways from the methods described in the earlier papers. First, we used a mass spectrometer (MS) rather than a pressure gauge to account for room-temperature gas coming from the vacuum chamber walls whose condensation onto the QCM reduces the apparent mass loss rate. Second, we accounted for condensation of gas originating from other parts of the cold copper QCM mount that had not previously been considered. These two modifications are described in greater detail in the next subsections.

Mass spectrometer monitoring of chamber gas

As described in Grundy et al. (2024), gas in the vacuum chamber that arrives at and sticks to the QCM partially offsets the sublimation loss, leading to an underestimate of the vapor pressure unless it is accounted for. In previous works, we had corrected for this deposition by establishing a relationship between chamber pressure measured with a pressure gauge and the condensation mass flux onto the QCM. However, to fit the dependence on pressure measured at the gauge, we needed to include a term to account for the contribution from non-condensable contaminant gases such as hydrogen and nitrogen that were measured by the pressure gauge but did not freeze onto the QCM. This term was assumed to be constant on a given day. But that is not necessarily a good assumption, especially for something like hydrogen, which the ion gauge can produce as a fragment from hydrocarbon molecules being studied. In the current study, we used a Stanford Research Systems RGA-200 quadrupole mass spectrometer (MS) to monitor the chamber partial pressure for the specific gas being investigated, replacing the p_{gauge} measurement used in the earlier papers. This change eliminated confusion from the presence of non-condensable contaminants. The one exception was the case of N_2 during our studies of C_2H_4, since both molecules have masses of 28 Da, making them indistinguishable with the MS, since we only recorded the mass of the material being studied plus the masses of known contaminants like H_2, H_2O, and CO_2. However, we saw no evidence for an excess fall-off in condensation rates for low pressures of C_2H_4 as would have been expected if substantial N_2 contamination had been present in the system. Prior to deposition in our C_2H_2 experiments, the partial pressure of N_2 was observed to be below 10^{-9} Torr (10^{-7} Pa), from which we infer that its abundance would have been similar in the C_2H_4 experiments. Other condensable contaminants do exist in the system, chiefly H_2O, but the MS showed it too to be below 10^{-9} Torr, much lower than the gases being studied.

Condensation of gas from cold surfaces

Although we had accounted for gas arriving at the QCM from the room temperature walls of the vacuum chamber in Grundy et al. (2024), we did not account for gas arriving from cold parts of the apparatus. In our system, lines of sight exist between the quartz crystal and the copper face plate that holds it in place, as well as between the quartz crystal and the portion of the copper angle bracket bolted to the cold tip (see Grundy et al. 2024 Figure 1). Both of these regions are isothermal with the quartz crystal at T_QCM, so they should experience identical rates of sublimation. As derived in Appendix A, a portion of the apparatus at T_QCM and within the field of view of the QCM contributes to condensation onto the QCM by modifying the time rate of change in areal mass Q

$$\Delta \frac{dQ}{dt} \;=\; p_\mathrm{vap}\left(T_\mathrm{QCM}\right)\sqrt{\frac{M}{2\pi R T_\mathrm{QCM}}}\int \frac{\cos\theta}{\pi}\,d\Omega \qquad \text{(Eq. 1)}$$

where $\Delta\, dQ/dt$ indicates the change in dQ/dt resulting from this source of condensation, M is the molar mass, R is the gas constant, and the integral accounts for the portion of the QCM's field of view filled by this part of the apparatus, with $d\Omega$ as the element of solid angle and θ as the angle where that element is located relative to a vector normal to the QCM. This expression assumes all molecules incident on the QCM stick to it, which should be a good assumption for the low velocities at which molecules depart cold surfaces.

Folding this additional condensation source into the Grundy et al. (2024) expression for net change in areal mass, we obtain

$$\frac{dQ}{dt} \;=\; -p_\mathrm{vap}\left(T_\mathrm{QCM}\right)\sqrt{\frac{M}{2\pi R T_\mathrm{QCM}}}\left(1-\int \frac{\cos\theta}{\pi}\,d\Omega\right) \;+\; \Phi p_\mathrm{MS}\sqrt{\frac{M}{2\pi R T_\mathrm{room}}}\;, \qquad \text{(Eq. 2)}$$

where p_MS is the chamber partial pressure measured by the MS and Φ is the polynomial scaling applied to p_MS to match the separately measured deposition of chamber gas onto the QCM. This equation can be rearranged to solve for p_vap at T_QCM

$$p_\mathrm{vap}\left(T_\mathrm{QCM}\right) \;=\; \frac{\Phi p_\mathrm{MS}\sqrt{\dfrac{T_\mathrm{QCM}}{T_\mathrm{room}}} \;-\; \dfrac{dQ}{dt}\sqrt{\dfrac{2\pi R T_\mathrm{QCM}}{M}}}{1-\displaystyle\int \frac{\cos\theta}{\pi}\,d\Omega}\;. \qquad \text{(Eq. 3)}$$

This equation is the same as Grundy et al. (2024) Eq. 6 except for the denominator. Note that the denominator has no temperature dependence. It is a constant multiplicative factor that we will call c_cold. For a specific laboratory setup, it depends only on the geometry of what parts of the QCM's field of view are filled with other surfaces at the same temperature.

To compute the value of this correction factor for our system, we measured the dimensions from photographs so as not to break vacuum. We estimated the $c_\mathrm{cold} = (1 - \int\cos(\theta)d\Omega/\pi)^{-1}$ correction factor to be 1.19 ± 0.03 (see details in Appendix A). Since this effect was not accounted for in our earlier papers (Blakley et al. 2024; Grundy et al. 2024), and the geometry of our system remains unchanged, the vapor pressures reported in those papers should all be multiplied by our c_{cold} value of 1.19.

Experiments

We performed experiments with the three C2 hydrocarbon species, ethane (C_2H_6), ethylene (C_2H_4), and acetylene (C_2H_2). Our C_2H_6 was supplied by Matheson®, with a reported purity of 99.99 %. C_2H_4 was also from Matheson, with a reported 99.995 % purity. C_2H_2 was industrial grade, supplied by Airgas®, but was passed through a pair of Entegris® gas purification units (GPU TX and WX series models) to remove the two main contaminants, water and acetone.

Each experiment involved a deposition phase followed by a warm up, and then a sublimation phase. During the deposition phase, we held the QCM at 40 K, a temperature sufficiently low that all molecules of the hydrocarbon being studied freeze onto the QCM upon arrival, with negligible sublimation. We recorded the deposition mass flux as a function of p_{MS}, between 10^{-8} to 10^{-5} Torr (10^{-6} to 10^{-3} Pa). This p_{MS} partial pressure is that of the species under study as measured with the MS. Later, we used a polynomial fit to the relation between pressure and deposition mass flux to correct for the deposition from room temperature gas in the chamber as a function of the partial pressure being monitored by the MS during sublimation.

After depositing an ice film, we turned off the closed-cycle helium refrigerator and allowed the cold head to warm passively for several minutes until the chamber pressure reached a maximum and started to drop again. This warming phase sublimated ice that had condensed onto warmer parts of the cold head, chiefly the first stage and the thermal shroud attached to it, leading to additional ice deposition onto the QCM at rates similar to the initial deposition, since the maximum pressure reached was generally within the same range we had used for deposition. If we did not drive the ice off of the shroud in this way, its sublimation during the subsequent part of the experiment would have been an additional small source of condensation onto the QCM that could not be easily corrected for, since we have no direct measurement of the temperature of the shroud. It is a small effect, because the QCM has a very limited line of sight view of the shroud, and none of the first stage. Nonetheless, preemptively removing excess ice from these portions of the apparatus after every deposition led to quicker stabilization of pressure after arriving at a new temperature.

Finally, we turned the refrigerator back on, and controlled to a temperature where net sublimation occurs. After the QCM temperature stabilized (about a minute after the diode thermometers showed stable temperatures) and p_{MS} had also stabilized, we recorded the QCM frequency simultaneously with p_{MS} from the MS at 3 second intervals for a few minutes (e.g., Blakley et al. 2024). We then changed to another temperature, and repeated until the ice sample had sublimated away. We limited our ice films to a maximum of 5 µm thickness (assuming ice densities between 0.6 and 0.8 g cm^{-3}, e.g., van Nes & Vos 1978; Satorre et al. 2017) and performed multiple deposition, warming, and sublimation cycles to collect data at higher temperatures where the ice was rapidly lost to sublimation.

We repeated our vapor pressure measurements for each species on at least two days in case instrument performance drifted over time. We also made multiple measurements for each temperature on each day, using various ice thicknesses up to 5 µm along with various thermal histories (stepping up or stepping down in temperature) to obtain an estimate of our measurement uncertainty. The standard deviations of p_{vap} from these repeated tests indicated experimental measurement uncertainties of ±7 %. An additional systematic uncertainty regarding the c_{cold} correction for condensation from other cold parts of the apparatus of ±3 % resulted in a total uncertainty of around ±10 % (we summed them rather than combining them in quadrature since one was a random error and one was systematic). An additional uncertainty came from the calibration of the temperature measurement, which we estimated as approximately ±0.2 K (see Grundy et al. 2024 for more details of the temperature calibration).

Results and Discussion

Fig. 1 shows vapor pressures p_{vap} as a function of temperature for the three hydrocarbon ices measured via the methodology described in the previous section. We also plotted the widely-used polynomial expressions from Fray & Schmitt (2009). For C_2H_4 and C_2H_6, our points differ little from the Fray & Schmitt expressions and from other experiments using methods similar to ours (Millán et al. 2024). Our results for C_2H_2 are more discrepant, falling about an order of magnitude below the polynomial approximation recommended by Fray & Schmitt, although they are consistent with the trend of the Tickner & Lossing (1951) data. We attribute this discrepancy to the existence of a lower temperature orthorhombic solid phase that is stable below 133 K (e.g., Sugawara & Kanda 1952; McMullan et al. 1992; Peng et al. 2023). See Appendix B for discussion on the solid-solid transition point at 133 K.

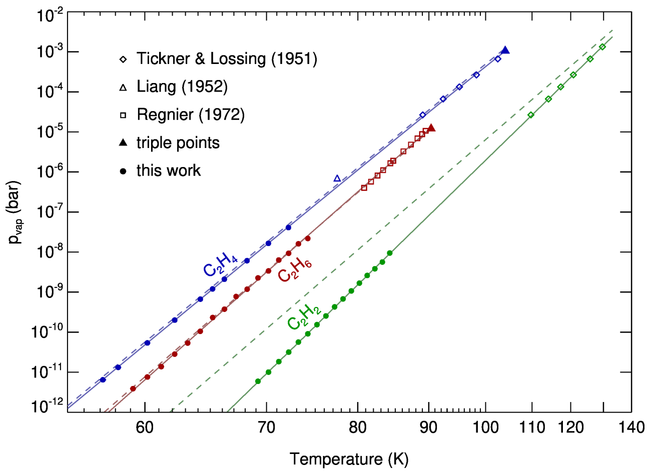

Figure 1: Our measured vapor pressures (circles) compared with polynomial expressions from Fray & Schmitt (2009, dashed curves). Temperatures are plotted on a scale that is linear in 1/*T*. Our estimated uncertainties (±10 % in p_{vap} and ±0.2 K in temperature) are smaller than the plotted points. Solid curves are fits of the Clausius-Clapeyron equation (for C_2H_2) and the Lobo & Ferreira sublimation equation (for C_2H_4 and C_2H_6).

Using the Clausius-Clapeyron relation for the change in pressure with temperature as a function of pressure p, temperature T, and latent heat of sublimation L, we solved for a best-fit constant L along with a pressure p_0 corresponding to an arbitrary reference temperature T_0 selected near the middle of our range of measurements, using our full set of vapor pressure measurements for that species plus higher temperature literature measurements. These include data from Regnier (1972) for C_2H_6 and from Tickner & Lossing (1951) for C_2H_2 and C_2H_4. We only used the literature data for temperatures below the triple points of C_2H_4 and C_2H_6 and below the 133 K solid-solid phase transition of C_2H_2. For the Tickner & Lossing data, we also limited our used of literature vapor pressures to those measured as above 0.02 Torr (2.7 Pa) where a thermal transpiration correction is not needed (Liang 1952). The values thus obtained are shown in Table 1 along with uncertainties arising from the Monte Carlo bootstrap method for the estimated ±10 % uncertainties in p_{vap}. These L values can be compared to the National Institute of Standards and Technology (NIST) values in the last column of the table (Regnier 1972; Stephenson & Malanowski 1987; see also Acree Jr. & Chickos 2015; Yu et al. 2023).

Table 1

Constant Latent Heat

Species	T_0 (K)	p_0 (bar)	L (kJ mol^{-1})	L_{NIST} (kJ mol^{-1})
C_2H_2	77	$(3.8 \pm 0.1) \times 10^{-10}$	23.8 ± 0.1	23.5
C_2H_4	64	$(6.0 \pm 0.2) \times 10^{-10}$	20.0 ± 0.1	18.4
C_2H_6	67	$(6.0 \pm 0.1) \times 10^{-10}$	21.5 ± 0.1	22.6

A temperature-dependent latent heat of sublimation can be obtained using the methods of Lobo & Ferreira (2001), as described in Grundy et al. (2024) and shown in Figure 2. This uses additional parameters derived from the isobaric heat capacities of solid phase and ideal gas from the literature, information that is only available for C_2H_4 and C_2H_6 (Egan & Kemp 1937; Din 1961). The Lobo & Ferreira A and B parameters fitted to our data plus the literature data for temperatures below the triple point appear in Table 2, along with the additional C, D_2, D_3, and D_4, parameters derived from literature values. For C_2H_2 we fitted the first two parameters (A_0 and A_1) of the Fray & Schmitt first-order polynomial which equates to the Clausius-Clapeyron equation $p_{vap}(T) = \exp(A_0 + A_1/T)$.

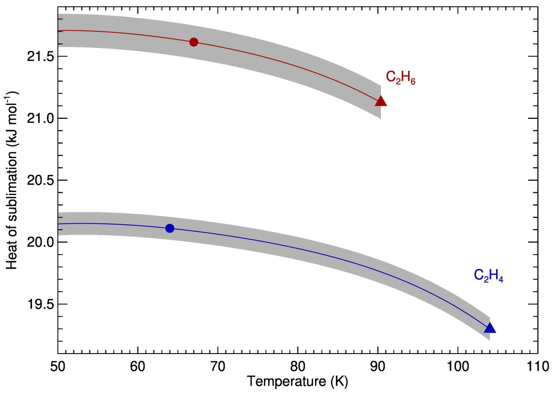

Figure 2: Temperature-dependent heat of sublimation of C_2H_4 and C_2H_6 ices derived from the Lobo & Ferreira equation using the parameters in Table 2. Triangles are heats at the triple points; circles are heats at reference temperatures T_0 in Table 1. Gray bands reflect the uncertainty in the B parameter.

The fit for C_2H_4 and C_2H_6 may be tested to calculate the heat of sublimation at their triple points, (104.0 ± 0.1) K and (90.34 ± 0.01) K, respectively (Fray & Schmitt, 2009) and then compared with literature data. As also plotted on Figure 2, the heats are calculated to be (19.3 ± 0.1) kJ/mol and (21.1 ± 0.1) kJ/mol, respectively. For C_2H_4, based on the heat of fusion 800.8 cal/mol (= 3.35 kJ/mol) by Egan & Kemp (1937) and the heat of evaporation 15.92 kJ/mol by NIST at the triple point, we can sum these to obtain the heat of sublimation as 19.27 kJ/mol. For C_2H_6,

Table 2

Parameters for Fray & Schmitt (C_2H_2) and Lobo & Ferreira (C_2H_4 and C_2H_6) expressions

Fray & Schmitt parameter [units]	**C_2H_2**	**Lobo & Ferreira parameter [units]**	**C_2H_4**	**C_2H_6**
A_0	**15.47 ± 0.13**	A	**−67.55 ± 0.15**	**−65.80 ± 0.16**
A_1 [K]	**−2861 ± 10**	B [K]	**1988 ± 11**	**2191 ± 12**
		C	24.44	24.57
		D_2 [K^{-1}]	−0.5048	−0.5315
		D_3 [K^{-2}]	2.320×10^{-3}	2.583×10^{-3}
		D_4 [K^{-3}]	-5.61×10^{-6}	-6.71×10^{-6}

Table note: bold figures are our fitted values and their 1-σ uncertainties. Other Lobo & Ferreira parameters were derived from literature values.

based on the heat of fusion 682.9 cal/mol (= 2.86 kJ/mol) by Witt & Kemp (1937) and the heat of evaporation 17.88 kJ/mol by NIST at the triple point, the heat of sublimation is 20.74 kJ/mol. Upon comparison, the calculations match the literature data within 0.1 kJ/mol for C_2H_4 and 0.4 kJ/mol for C_2H_6, which are all below 2 % error.

For C_2H_2, as the vapor pressure is fitted to the Clausius-Clapeyron equation, the heat of sublimation is constant and can be derived solely from its parameter A_1. For temperatures below the solid-solid phase-transition point of 133 K, the fitted A_1 parameter in Table 2 gives the heat of sublimation for the low-temperature solid, i.e., (23.8 ± 0.1) kJ/mol. Based on the heat of solid-solid phase transition 607 cal/mol (= 2.54 kJ/mol) at 133 K by Miskiewicz et al. (1976), we can readily calculate the heat of sublimation of the high-temperature solid to be 21.28 kJ/mol. This value is comparable to the heat derived from parameter A_1 by Fray & Schmitt (2009), i.e., 21.08 kJ/mol.

Applying the same $c_{\text{cold}} = 1.19$ correction factor to our previously published vapor pressures (Blakley et al. 2024; Grundy et al. 2024), we obtained updated Lobo & Ferreira A and B parameters for those species as listed in Table 3. Although the correction for back condensation from room temperature chamber gas was estimated differently in those papers, our new correction for back condensation from cold parts of the apparatus is independent of that correction and is equally applicable to those results.

Table 3

Updated Lobo & Ferreira A and B parameters

	α N_2	**α CO**	**CH_4 I**	**β O_2**	**NH_3**
A	−3.35 ± 0.19	−6.150 ± 0.036	−2.666 ± 0.027	14.85 ± 0.23	−5.73 ± 0.57
***B* [K]**	817 ± 5	971.6 ± 2.1	1127.8 ± 2.0	1147 ± 9	3570 ± 27

Summary

We present two improvements on the Grundy et al. (2024) quartz crystal microbalance method for measuring vapor pressures of volatile ices in the low pressure range between about 10^{-11} and 10^{-7} bar (10^{-6} and 10^{-2} Pa). These involve using a mass spectrometer in place of a pressure gauge to account for back condensation of room temperature gas from the chamber onto the quartz crystal and also a geometric correction for back condensation from other parts of the apparatus that are at the same low temperature as the quartz crystal. We apply the updated methodology to measure vapor pressures of ices of the C2 hydrocarbons C_2H_2, C_2H_4, and C_2H_6, and also provide updated values for five other important outer Solar System volatile species (N_2, CO, CH_4, O_2, and NH_3) that we had published previously without accounting for the c_{cold} geometric correction factor.

Data Availability

All laboratory data that we used to derive the results presented in this paper are publicly archived along with the values plotted in the figures at [URL to be finalized on acceptance]. The data consist of time series ASCII files listing calibrated temperatures, partial pressures, and QCM frequencies. Values shown in the figures include our measurements and literature measurements of vapor pressure and enthalpy of sublimation versus temperature including both measured discrete values plotted as points and the polynomials plotted as smooth curves.

Acknowledgments

Portions of this work and the Astrophysical Materials Laboratory facility at Northern Arizona University were supported by NASA Solar System Workings Program grants 80NSSC19K0556 and 80NSSC25K7114; by the State of Arizona Technology and Research Initiative Fund (TRIF), administered by the Arizona Board of Regents; by NSF Research Experience for Undergraduates grant 1950901 to Northern Arizona University; and by philanthropic donations from the John and Maureen Hendricks Foundation, from Lowell Observatory’s Slipher Society, and from the Joe Marcus Cometary Research fund. We are grateful to two anonymous reviewers for their constructive suggestions that helped to improve this manuscript. We also thank the free and open source software communities for empowering us with key tools used to complete this project, notably Linux, the GNU tools, LibreOffice, Evolution, Python, the Astronomy Users Library, and FVWM.

Appendix A

Here we derive an expression for the intensity of the mass flux from a source sublimating with dQ_{source}/dt (mass per unit area per second) as given by the Hertz-Knudsen-Langmuir equation (e.g., Langmuir 1913). Assuming diffuse scattering behavior (Lambertian emission), such that intensity at an angle θ from normal to the source $I(r,\theta)$ goes as $\cos\theta$, and intensity drops off following an inverse square law with distance r, we can assume a mathematical structure for the intensity profile of $I(r,\theta) = D(dQ_{\mathrm{source}}/dt)(\cos\theta/\mathrm{r}^2)$, where D is a constant that we need to solve for. To do this, we note that if we integrate the intensity over a shell that fully encloses the source, the total flux should integrate to dQ_{source}/dt. Thus $dQ_{\mathrm{source}}/dt = \int I(r,\theta)d\Omega$ where $d\Omega$ is the element of solid angle. Replacing $I(r,\theta)$ with $D(dQ_{\mathrm{source}}/dt)(\cos\theta/r^2)$, and dividing both sides by dQ_{source}/dt, we have $1 = D\int\cos\theta\, r^{-2}\, d\Omega$, which, integrated over the 2π sr that the source can sublimate into evaluates as πD, so we conclude that $D = 1/\pi$ and $I(r,\theta) = dQ_{\mathrm{source}}/dt \cos\theta / \pi r^2$.

To convert this to deposition rate arriving at the QCM as a function of solid angle Ω in its field of view, we note that if a circular unit area is located sufficiently far from the source that the area of the spherical cap approaches that of its bounding circle, and if we assume that the area is sufficiently small that the intensity $I(r,\theta)$ varies little from one edge of the area to the other, and similarly that the subliming source is sufficiently small/far such that its intensity does not vary much from one edge to the other, we can make a series of approximations that enables us to convert this expression to one that is a function of solid angle, rather than distance. In this limit, the solid angle of the unit-area spherical cap at a distance r is r^{-2}. Thus,

$$\frac{dQ_{\mathrm{target}}}{dt} = \frac{dQ_{\mathrm{source}}}{dt}\frac{\cos\theta}{\pi}\Omega = p_{\mathrm{vap}}(T_{\mathrm{QCM}})\sqrt{\frac{M}{2\pi RT}}\frac{\cos\theta}{\pi}\Omega\ , \qquad \text{(Eq. A1)}$$

where Ω is the solid angle of the source as seen from the target.

As a test, consider the limiting case where the entire 2π sr field of view of the QCM is filled, equivalent to having the QCM inside of an enclosed, isothermal container. In that case, sublimation from and condensation onto the QCM should exactly balance, since there should be no net migration of material. This is confirmed since the integral of $\cos(\theta)d\Omega/\pi$ over 2π sr equals unity, leaving the condensation equivalent to dQ/dt from the Hertz-Knudsen-Langmuir equation for sublimation.

For our system, the copper collar around the quartz crystal extends from the horizon as seen from the center of the crystal up to approximately 16 degrees elevation. The upper part of the angle bracket connecting the QCM mount to the second stage tip of the refrigerator rises to 43 degrees elevation as seen from the center of the crystal, and its azimuthal width is about 76 degrees. These angles are approximate, having been measured from photographs to avoid breaking vacuum. Using these angles, we can integrate to obtain the correction factor $c_{\mathrm{cold}} = (1 - \int\cos(\theta)d\Omega/\pi)^{-1} = 1.19 \pm 0.03$, where the uncertainty comes from assuming ±2.5 degree measurement uncertainties on each of the angles. We varied the three angles randomly over ±2.5° 1-σ Gaussian distributions centered on each measurement and repeated the integral 10,000 times to assess the uncertainty in our estimate of c_{cold} for our system.

Appendix B

As mentioned in the paper, acetylene has a solid-solid phase transition at 133 K (McMullan et al., 1992). Unfortunately, this work was designed only to make measurements at much lower temperatures, so that we cannot confirm this transition temperature. However, we can still give a temperature range for the transition point based only on the sublimation vapor pressures that we and others did. When a solid changes to a different crystalline structure, i.e., a different solid phase, the behavior of the vapor pressure must also change accordingly, which is reflected by an abrupt change in slope on the Clausius-Clapeyron phase diagram. In other words, the transition point is the intersection between two lines that represent two different solid phases.

Fray & Schmitt (2009) fitted two sets of experimental vapor-pressure data by Burrel & Robertson (1915) and McIntosh (1907). There are two data points below the solid-solid transition temperature of 133 K, both of which are not used here for the Clausius-Clapeyron (C-C) fitting over the vapor pressures of high-temperature cubic solid.

Though Fray & Schmitt mentioned using all 26 data points in their C-C fitting in their Table 4, it turns out that they did not include one data point at the lowest temperature, which is indeed far off the trend of the other data (see the left-hand panel of Figure 3). It seems that Burrell & Robertson detected the phase transition but failed to recognize it. The resulting parameters are listed in Fray & Schmitt's Table 5, and here we present them with the fitting errors:

$A_0 = 13.40 \pm 0.06$

$A_1 = –2536 \pm 11$ [K]

Since they did not consider the presence of the low-temperature orthorhombic solid below 133 K, we refitted the parameters after excluding two data points that lie below 133 K:

$A_0 = 13.46 \pm 0.07$

$A_1 = –2548 \pm 13$ [K]

We use these parameters and the errors to draw the two lines representing the maximum and minimum sublimation vapor pressures from the fitting (see the left panel of Figure 3). Note here, that the triple point lies between these two lines as it should.

For the low-temperature orthorhombic solid we worked on, we use the C-C parameters and their errors listed in Table 2 to draw the two lines representing the maximum and minimum sublimation vapor pressures due to the fitting errors (see the middle panel of Figure 3). There are 6 data points of Tickner & Lossing (1951) below 133 K that we included in our C-C fitting, also plotted in Figure 1. The other 3 data points above 133 K belong to the cubic solid; they are plotted in Figure 3 just for completeness.

When the two pairs of lines representing different solid phases are plotted together (right panel of Figure 3), their intersections give us the temperature range that constrains the location of the true solid-solid transition point, i.e., between 131.1 K and 185.5 K. As expected, this temperature range does have the measured transition temperature of 133 K in it. If one chose Fray & Schmitt's parameters instead of ours for the cubic solid, however, the temperature range would slightly shift to 134.5-194.0 K, thus excluding the measured transition temperature. This shift is due to the inclusion of one data point right below 133 K in Fray & Schmitt's fitting.

It is also worth noting here that data by Tickner & Lossing (1951) below 133 K, which sit nicely in the low-temperature fitting as shown in the middle panel of Figure 3, will be overestimated if one uses the high-temperature fitting as seen in the right panel of Figure 3. The larger slope tells us that the heat of sublimation of the orthorhombic solid acetylene is larger than that of the cubic one.

References

Acree Jr., W., and J.S. Chickos 2015. Phase transition enthalpy measurements of organic and organometallic compounds. Sublimation, vaporization and fusion enthalpies from 1880 to 2015. Part 1. C1 - C10. *J. Phys. Chem. Ref. Data* 45, 033101.

Arabhavi, A.M., et al. (42 co-authors) 2024. Abundant hydrocarbons in the disk around a very-low-mass star. *Science* 384, 1086-1090.

Bair, A.N., and D.G. Schleicher 2025. Comprehensive analyses of the strongly carbon-chain depleted comets in Lowell Observatory's narrowband photometry database. *Planetary Sci. J.* 6, 248.

Blakley, B.P., W.M. Grundy, J.K. Steckloff, S.P. Tan, J. Hanley, A.E. Engle, S.C. Tegler, G.E. Lindberg, S.M. Raposa, K.J. Koga, and C.L. Thieberger 2024. The equilibrium vapor pressures of ammonia and oxygen ices at outer solar system temperatures. *Planetary & Space Sci.* 244, 105863.

Brown, G.N., and W.T. Ziegler 1980. Vapor pressure and heats of vaporization and sublimation of liquids and solids of interest in cryogenics below 1-atm pressure. *Adv. Cryo. Eng.* 25, 662-670.

Brown, R.H., L.A. Soderblom, J.M. Soderblom, R.N. Clark, R. Jaumann, J.W. Barnes, C. Sotin, B. Buratti, K.H. Baines, and P.D. Nicholson 2008. The identification of liquid ethane in Titan's Ontario Lacus. *Nature* 454, 607-610.

Burrell, G.A., and I.W. Robertson 1915. The vapor pressures of acetylene, ammonia and isobutane at temperatures below their normal boiling points. *J. Am. Chem. Soc.* 37, 2482-2486.

Carrascosa, H., G.A. Cruz-Díaz, G.M. Muñoz Caro, E. Dartois, and Y.J. Chen 2020. Photon-induced desorption of larger species in UV-irradiated methane ice. *Mon. Not. R. Astron. Soc.* 493, 821-829.

Cheng, A.F., M.E. Summers, G.R. Gladstone, D.F. Strobel, L.A. Young, P. Lavvas, J.A. Kammer, C.M. Lisse, A.H. Parker, E.F. Young, S.A. Stern, H.A. Weaver, C.B. Olkin, and K. Ennico 2017. Haze in Pluto's atmosphere. *Icarus* 290, 112-133.

Clark, R.N., J.M. Curchin, J.W. Barnes, R. Jaumann, L. Soderblom, D.P. Cruikshank, R.H. Brown, S. Rodriguez, J. Lunine, K. Stephan, T.M. Hoefen, S. Le Mouélic, C. Sotin, K.H. Baines, B.J. Buratti, and P.D. Nicholson 2010. Detection and mapping of hydrocarbon deposits on Titan. *J. Geophys. Res.* 115, E10005.

Colmenares, M.J., et al. (18 co-authors) 2024. JWST/MIRI detection of a carbon-rich chemistry in the disk of a solar nebula analog. *Astrophys. J.* 977, 173.

Cordier, D., J.W. Barnes, and A.G. Ferreira 2013. On the chemical composition of Titan's dry lakebed evaporites. *Icarus* 226, 1431-1437.

Czaplinski, E.C., W.A. Gilbertson, K.K. Farnsworth, and V.F. Chevrier 2019. Experimental study of ethylene evaporites under Titan conditions. *ACS Earth Space Chem.* 3, 2353-2362.

Din, F. 1961. *Thermodynamic Functions of Gases: Methane, nitrogen, ethane*. Vol. 3.

Butterworths Scientific Publications.

Egan, C.J., and J.D. Kemp 1937. Ethylene. The heat capacity from 15 K to the boiling point. The heats of fusion and vaporization. The vapor pressure of the liquid. The entropy from thermal from thermal measurements compared with the entropy from spectroscopic data. *J. Amer. Chem. Soc.* 59, 1264-1268.

Emery, J.P., I. Wong, R. Brunetto, J.C. Cook, N. Pinilla-Alonso, J.A. Stansberry, B.J. Holler, W.M. Grundy, S. Protopapa, A.C. Souza-Feliciano, E. Fernández-Valenzuela, J.I. Lunine, and D.C. Hines 2024. A tale of 3 dwarf planets: Ices and organics on Sedna, Gonggong, and Quaoar from JWST spectroscopy. *Icarus* 414, 116017.

Feng, L., et al. (22 co-authors) 2025. The first JWST view of a 30-Myr-old protoplanetary disk reveals a late-stage carbon-rich phase. *Astrophys. J. Lett.* 978, L30.

Fray, N., and B. Schmitt 2009. Sublimation of ices of astrophysical interest: A bibliographic review. *Planet. Space Sci.* 57, 2053-2080.

Gladstone, G.R., and L.A. Young 2019. New Horizons observations of the atmosphere of Pluto. *Ann. Rev. Earth Planet. Sci.* 47, 119-140.

Grundy, W.M., et al. (39 co-authors) 2016. Formation of Charon’s red poles from seasonally cold-trapped volatiles. *Nature* 539, 65-68.

Grundy, W.M., S.C. Tegler, J.K. Steckloff, S.P. Tan, M.J. Loeffler, A.V. Jasko, K.J. Koga, B.P. Blakley, S.M. Raposa, A.E. Engle, C.L. Thieberger, J. Hanley, G.E. Lindberg, M.D. Gomez, and A.O. Madden-Watson 2024. Laboratory measurement of volatile ice vapor pressures with a quartz crystal microbalance. *Icarus* 410, 115767.

Hirtzig, M., T. Tokano, S. Rodriguez, S. Le Mouélic, and C. Sotin 2009. A review of Titan’s atmospheric phenomena. *Astron. & Astrophys. Rev.* 17, 105-147.

Hoey, W.A., S.K. Yeoh, L.A. Trafton, D.B. Goldstein, and P.L. Varghese 2017. Rarefied gas dynamic simulation of transfer and escape in the Pluto-Charon system. *Icarus* 287, 87-102.

Hörst, S.M. 2017. Titan’s atmosphere and climate. *J. Geophys. Res. E* 122, 432-482.

Houge, A., A. Johansen, E. Bergin, F.J. Ciesla, B. Bitsch, M. Lambrechts, T. Henning, and G. Perotti 2025. Burned to ashes: How the thermal decomposition of refractory organics in the inner protoplanetary disc impacts the gas-phase C/O ratio. *Astron. & Astrophys.* 699, A227.

Hudson, R.L., M.H. Moore, and L.L. Raines 2009. Ethane ices in the outer Solar System: Spectroscopy and chemistry. *Icarus* 203, 677-680.

Langmuir, I. 1913. The vapor pressure of metallic tungsten. *Phys. Rev.* 2, 329-342.

Lavvas, P., E. Lellouch, D.F. Strobel, M.A. Gurwell, A.F. Cheng, L.A. Young, and G.R. Gladstone 2021. A major ice component in Pluto’s haze. *Nature Astron.* 5, 289-297.

Liang, S.C., 1952. Low vapor pressure measurement and thermal transpiration. *J. Phys. Chem.* 56, 660-662.

Lobo, L.Q., and A.G.M. Ferreira 2001. Phase equilibria from the exactly integrated Clapeyron equation. *J. Chem. Thermodynamics* 33, 1597-1617.

Mastrogiuseppe, M., A.G. Hayes, V. Poggiali, J.I. Lunine, R.D. Lorenz, R. Seu, A. Le Gall, C.

Notarnicola, K.L. Mitchell, M. Malaska, and S.P.D. Birch 2018. Bathymetry and composition of Titan's Ontario Lacus derived from Monte Carlo-based waveform inversion of Cassini RADAR altimetry data. *Icarus* 300, 203-209.

McIntosh, D. 1907. The physical properties of liquid and solid acetylene. *J. Phys. Chem.* 11, 306-317.

McMullan, R.K., A. Kvick, and P. Popelier 1992. Structure of cubic and orthorhombic phases of acetylene by single-crystal neutron diffraction. *Acta Cryst.* B48, 726-731.

Menaucourt, J. 1982. Pression de vapeur saturante de l'ethylene entre 77 K et 119 K. *J. Chim. Phys.* 79, 531–535.

Millán, C., R. Luna, M. Domingo, C. Santonja, and M.Á. Satorre 2024. Experimental vapor pressure determination for C_2H_4, C_2H_6, CH_3OH, CH_4, CO, CO_2, H_2O, and N_2 molecules for astrophysical relevant temperatures. Implications for the presence of volatiles in Kuiper belt objects and trans-neptunian objects. *Astrophys. J.* 970, 117.

Miskiewicz, S., K. Rieser, and T. Dorfmüller 1976. Thermodynamische Untersuchungen an kondensierten Phasen. *Ber. Bunsenges. Phys. Chem.* 80, 395-405.

Nixon, C.A. 2024. The composition and chemistry of Titan's atmosphere. *ACS Earth Space Chem.* 8, 406-456.

Paganini, L., M.N. Camarca, M.J. Mumma, S. Faggi, M. Lippi, and G.L. Villanueva 2019. Observations of Jupiter family comet 252P/LINEAR during a close approach to Earth reveal large abundances of methanol and ethane. *Astron. J.* 158, 98.

Peng, J., S. Zhang, K. Refson, and M.T. Dove 2023. Unique features of the structural phase transition in acetylene showing simultaneous characteristics of reconstructive, displacive and order-disorder. *Phys. Chem. Chem. Phys.* 25, 9909-9924.

Protopapa, S., et al. (18 co-authors) 2025. JWST detection of hydrocarbon ices and methane gas on Makemake. *Astrophys. J. Lett.* 991, L34.

Raut, U., B.D. Teolis, J.A. Kammer, C.J. Gimar, J.S. Brody, G.R. Gladstone, C.J.A. Howett, S. Protopapa, and K.D. Retherford 2022. Charon's refractory factory. *Science Adv.* 8, eabq5701.

Regnier, J. 1972. Tension de vapeur de l'éthane entre 80 et 135° K. *J. Chim. Phys.* 69, 942-944.

Satorre, M.Á., C. Millán, G. Molpeceres, R. Luna, B. Maté, M. Domingo, R. Escribano, C. Santonja 2017. Densities and refractive indices of ethane and ethylene at astrophysically relevant temperatures. *Icarus* 296, 179-182.

Stephenson, R.M., and S. Malanowki 1972. Properties of Organic Compounds. In: *Handbook of the Thermodynamics of Organic Compounds*. Springer, Dordrecht.

Sugawara, T., and E. Kanda 1952. The crystal structure of acetylene. I. *Sci. Rept. Res. Inst. Tohoku Univ. Ser A* 4, 607-614.

Tabone, B., et al. (44 co-authors) 2023. A rich hydrocarbon chemistry and high C to O ratio in the inner disk around a very low-mass star. *Nature Astron.* 7, 805-814.

Teolis, B., U. Raut, J.A. Kammer, C.J. Gimar, C.J.A. Howett, G.R. Gladstone, and K.D. Retherford 2022. Extreme exospheric dynamics at Charon: Implications for the red spot. *Geophys. Res. Lett.* 49, E97580.

Tickner, A.W., and F.P. Lossing 1951. The measurement of low vapor pressures by means of a mass spectrometer. *J. Phys. Chem.* 55, 733-740.

Tomasko, M.G., L. Doose, S. Engel, L.E. Dafoe, R. West, M. Lemmon, E. Karkoschka, and C. See 2008. A model of Titan's aerosols based on measurements made inside the atmosphere. *Planetary & Space Sci.* 56, 669-707.

van Nes, G.J.H., and A. Vos 1978. Single-crystal structures and electron density distributions of ethane, ethylene and acetylene. I. Single-crystal X-ray structure determinations of two modifications of ethane. *Acta Crystallogr., Sect. B: Struct. Sci.* 34, 1947-1956.

Witt, R.K., and J.D. Kemp 1937. The Heat Capacity of Ethane from 15 K. to the Boiling Point. The Heat of Fusion and the Heat of Vaporization. *J. Amer. Chem. Soc.* 59, 273-276.

Young, L.A., et al. (25 co-authors) 2018. Structure and composition of Pluto's atmosphere from the New Horizons solar ultraviolet occultation. *Icarus* 300, 174-199.

Yu, X., Y. Yu, J. Garver, J. Li, A. Hawthorn, E. Sciamma-O'Brien, X. Zhang, and E. Barth 2023. Material properties of organic liquids, ices, and hazes on Titan. *Astrophys. J. Supl. Ser.* 266, 30.

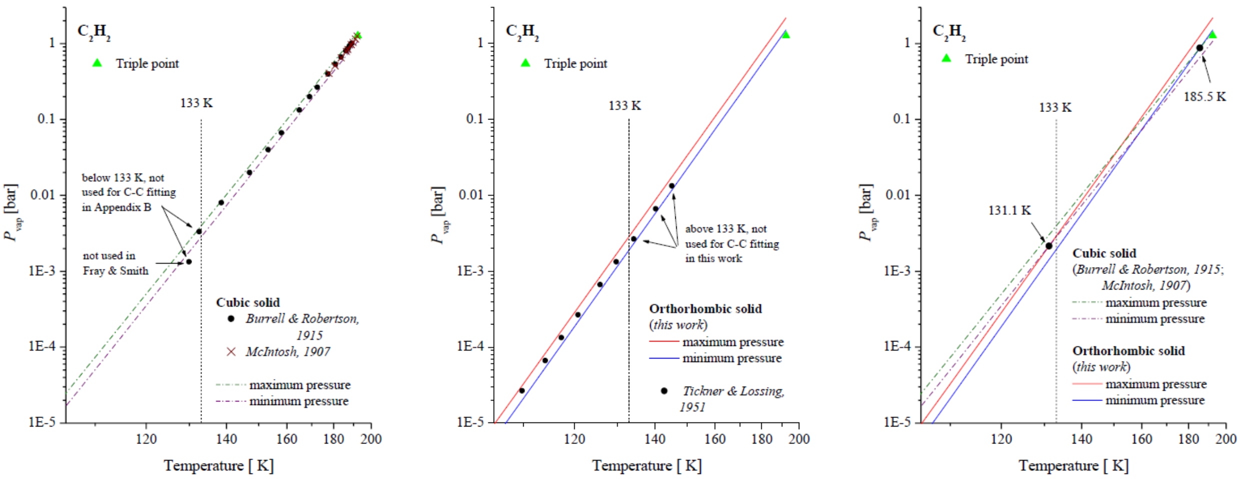

Figure 3. Sublimation vapor pressures (P_{vap}) of acetylene in the vicinity of solid-solid phase transition at 133 K. Maximum and minimum pressure lines result from the Clausius-Clapeyron fittings and the errors. See the text for the description of each panel.